Visualization and comparison of classical structures and quantum states of four-dimensional maps

Martin Richter, Steffen Lange, Arnd Bäcker, and Roland Ketzmerick
Technische Universität Dresden, Institut für Theoretische Physik and Center for Dynamics, 01062 Dresden, Germany
and Max-Planck-Institut für Physik komplexer Systeme, Nöthnitzer Straße 38, 01187 Dresden, Germany
(Received 7 November 2013; published 3 February 2014)

For generic 4D symplectic maps we propose the use of 3D phase-space slices, which allow for the global visualization of the geometrical organization and coexistence of regular and chaotic motion. As an example, we consider two coupled standard maps. The advantages of the 3D phase-space slices are presented in comparison to standard methods, such as 3D projections of orbits, the frequency analysis, and a chaos indicator. Quantum mechanically, the 3D phase-space slices allow for the comparison of Husimi functions of eigenstates of 4D maps with classical phase-space structures. This confirms the semiclassical eigenfunction hypothesis for 4D maps.

DOI: 10.1103/PhysRevE.89.022902 PACS number(s): 05.45.Mt, 03.65.Sq, 05.45.Jn

I. INTRODUCTION

Understanding higher-dimensional, dynamical systems, even with just a few particles, is a challenging task. Such systems are relevant in many areas of physics and chemistry [1], ranging from the dynamics of the solar system [2–4], dynamics of particle accelerators [5], to atoms and molecules [6–9]. Particular topics of interest concern the quantum signatures of Arnold diffusion [10–12] and quantum-classical correspondence in higher-dimensional mixed systems [13,14].

A standard example would be autonomous Hamiltonian systems with three degrees of freedom, which have a 6D phase space, which can be reduced to a 5D manifold due to energy conservation. Introducing a Poincaré section leads to a 4D symplectic map. This type of map also arises from time-periodically driven, Hamiltonian systems with two degrees of freedom, where a stroboscopic Poincaré section leads to a symplectic map acting on the 4D phase space. Such 4D maps are prototypical for the behavior of higher-dimensional systems, as they have the smallest possible dimension showing the essential difference to 2D symplectic maps: In 2D maps tori are one-dimensional and thus lead to absolute barriers of motion. In contrast, in 4D maps regular tori are two-dimensional manifolds in the 4D phase space, which cannot divide the phase space into dynamically distinct regions. One of the most fundamental consequences of this topological structure of 4D (and higher-dimensional) maps is that generically chaotic orbits can get arbitrarily close to any point in phase space, even if regular tori are present. One possible mechanism was constructed by Arnold [15], leading to the so-called Arnold diffusion [1,4,16,17]. Another striking phenomenon is the occurrence of power-law trapping of chaotic orbits in higher-dimensional systems with a mixed phase space [18–21], for which the mechanism is still an open question. While most of the analytical and numerical results about higher-dimensional systems have been obtained for the near-integrable case, many practical applications are concerned with generic systems, which cannot be described by perturbative methods; see, e.g., Refs. [22–24] and references therein.

For the lowest-dimensional Hamiltonian systems with regular and chaotic dynamics, such as 2D billiards or time-periodically driven 1D systems, the dynamics can be reduced to 2D symplectic maps. Their phase space can be easily visualized, providing substantial insight and intuition of the dynamics in phase space, such as chaotic motion, regular regions formed by 1D regular tori around stable periodic orbits, stable and unstable manifolds of unstable periodic orbits, nonlinear resonances, and hierarchical regions due to partial barriers at the border of the regular island. Also the time-evolution of trajectories can be visualized straightforwardly.

Such a direct visualization of the classical dynamics in phase space is also very useful when trying to understand the properties of the corresponding quantum mechanical system. According to the semiclassical eigenfunction hypothesis [25–27], one expects that eigenstates semiclassically concentrate on those regions in phase space that a generic orbit explores in the long-time limit. For ergodic systems this is proven by the quantum ergodicity theorem stating that almost all eigenfunctions become equidistributed in the semiclassical limit [28–30]. For systems with a mixed phase space one thus expects that (almost all) eigenstates either concentrate in the chaotic region or within the regular regions on the invariant tori. Away from the semiclassical limit this can be violated due to dynamical tunneling [31–34] and partial transport barriers [35]. The semiclassical eigenfunction hypothesis has been confirmed in several studies for 2D billiard systems and maps; see, e.g., Refs. [36–40] and references therein. In order to study this question for 4D maps, it is necessary to visualize the organization of phase space and in particular to display sets of individual tori.

For higher-dimensional systems a direct visualization of phase space is not possible.[1] Starting with the pioneering work of Froeschlé [43,44], several methods have been introduced to obtain a reduction to understand the dynamics. For example, two-dimensional plots of multisections [44,45] or projections to two [2,43,46,47] or three [48–50] dimensions, also including color to indicate the projected coordinate [51,52], frequency analysis [53–56], and action-space plots [57] . Further tools to investigate higher-dimensional phase spaces are chaos indicators to distinguish regular from chaotic motion, like finite-time Lyapunov exponents [58–60], fast Lyapunov indicator (FLI) [45,61,62], and many more; see, e.g., Refs. [63–65] and references therein.

[1] *You're just not thinking fourth dimensionally! – Right, right. I have a real problem with that*. (Quote from *Back to the Future Part III*).

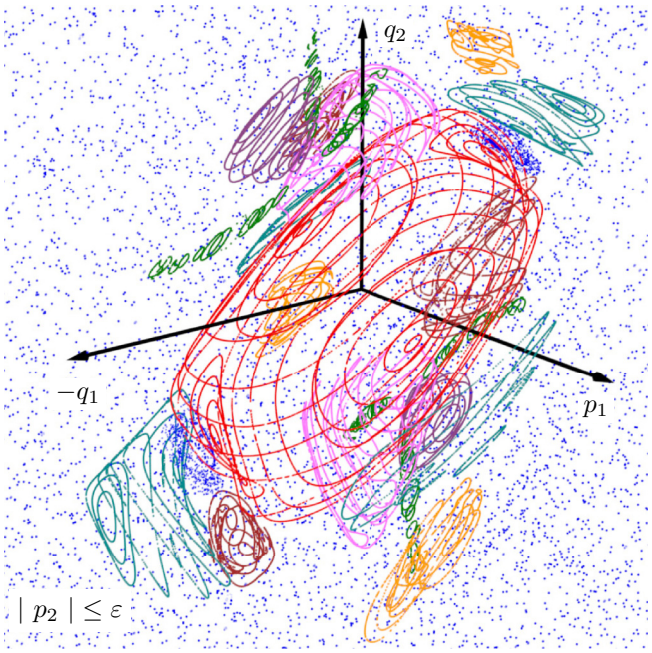

FIG. 1. (Color online) 3D phase-space slice $|p_2| \leqslant \varepsilon$ of the 4D map given by two coupled standard maps, Eq. (2), at strong coupling $\xi_{12} = 1$. Regular tori are given by 1D lines (red, cyan, violet, pink, green, orange, and brown). They are surrounded by chaotic orbits (blue dots). The central regular region (red) around the elliptic-elliptic fixed point is predominantly filled with regular tori (not shown for visual reasons). For a rotating view see the Supplemental Material [42].

The aim of this paper is to obtain a direct visual approach for an understanding of 4D symplectic maps similar to the insights already available for 2D maps. For this we propose the use of 3D phase-space slices; see Fig. 1 for an illustration of regular 2D tori and one chaotic orbit. We make use of the full dimensionality of the 3D slice by displaying and rotating it using standard 3D graphics. Since it is very instructive to see this rotation, for the convenience of the reader for all 3D phase-space slices in this paper videos with rotating camera position are given in the Supplemental Material [42]. The reduction from 4D to 3D is obtained by selecting those points of an orbit that lie in the 3D phase-space slice and plotting the remaining three coordinates. Thereby, 3D phase-space slices allow for displaying several different orbits at the same time and provide a global visualization of their arrangement in phase space. By this we are able to visualize quantum eigenstates of a generic system far away from integrability and compare them to the classical phase-space structures. This confirms the semiclassical eigenfunction hypothesis for regular and chaotic states in the case of 4D maps. Moreover, a combination of the 3D phase-space slices and the frequency analysis allows for identifying regular subregions and their separating resonance gaps. This also explains the nature of the so-called tube tori [50,52].

This paper is organized as follows: In Sec. II we introduce the 3D phase-space slices and the generic 4D symplectic map. The observations are compared with complementary methods, namely 3D projections, frequency analysis, and the fast Lyapunov indicator. In Sec. III we consider the quantum mechanics of 4D maps and the visualization of eigenstates by means of the Husimi function on the 3D phase-space slices. Finally, Sec. IV gives a summary and an outlook. Additionally, we discuss different slice conditions and combine 3D phase-space slices with a normal form transformation in the Appendix.

II. REGULAR PHASE-SPACE STRUCTURES

A. 3D phase-space slices

While the concept of 3D phase-space slices applies to arbitrary maps, we restrict our presentation to symplectic maps. For a symplectic map acting on a $2f$-dimensional phase space, an orbit started at an initial point leads to a sequence of points $(p_1,\ldots,p_f,q_1,\ldots,q_f)$. For $f \geqslant 2$ the dynamics cannot be displayed completely in a 2D or 3D figure. To obtain a visualization of the dynamics of higher-dimensional systems, we use of 3D phase-space slices Γ_ε, which are defined by thickening a 3D hyperplane Γ in the $2f$-dimensional phase space. To specify Γ, the simplest choice is to fix $2f-3$ coordinates from $p_1,\ldots,p_f,q_1,\ldots,q_f$. For 4D maps ($f = 2$), one thus has to fix one coordinate, e.g., $p_2 = p_2^*$, to define the slice by

$$\Gamma_\varepsilon = \{(p_1,p_2,q_1,q_2) \mid |p_2 - p_2^*| \leqslant \varepsilon\}. \tag{1}$$

Whenever a point of an orbit lies within Γ_ε, the remaining coordinates (p_1,q_1,q_2) are displayed in a 3D plot. This is different to the method by Froeschlé [43,44], which first projects onto the 3D phase space and then uses 2D slices to visualize this projection. Slice conditions like Eq. (1) have been considered, e.g., in Ref. [45], but without 3D visualization.

By the parameter ε the resolution of the resulting plot is controlled. Decreasing ε gives a tighter slice condition but also requires numerically computing longer trajectories as the slice condition is fulfilled less often. This also shows the necessity to consider a thickened hyperplane as in the limit $\varepsilon = 0$ a typical orbit will have no points in Γ_ε. Moreover, for a larger number of degrees of freedom this means that the orbit returns less often to the slice and also only a small part of phase space can be seen. Still it can be useful, if the dynamics is dominated by a few degrees of freedom. Using 3D visualization techniques [66], one can interactively explore the structure and dynamics of orbits in the 3D phase-space slice. Throughout this paper we focus on 4D symplectic maps and use $\varepsilon = 10^{-4}$.

For 4D symplectic maps we now discuss the expected visual appearance of the different objects in phase space: A typical chaotic trajectory fills a 4D volume in the 4D phase space. In the 3D phase-space slice this leads to a sequence of points filling a 3D volume. A typical regular torus is a 2D object embedded in the 4D phase space. In the 3D phase-space slice this will either lead to no points at all (i.e., the slice does not intersect the torus) or typically lead to two or more 1D lines. Periodic orbits usually will not be visible in the 3D phase-space slice. Only an appropriate choice of Γ will directly show periodic orbits; see Appendix 3 b. To understand this reduction from the 4D phase space to the 3D phase-space slice the analogous reduction of a 2D phase space to a 1D slice is helpful: Depending on the position of the slice, regular tori, which are 1D invariant curves, will either lead to 0 (no

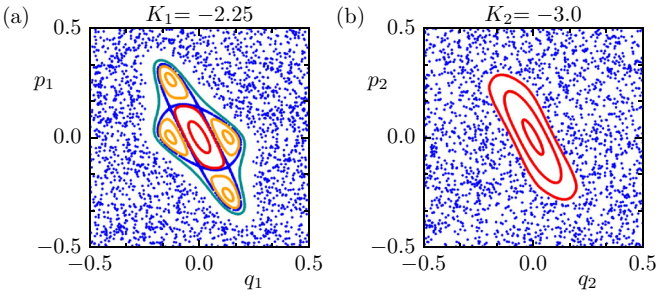

FIG. 2. (Color online) Phase space of the uncoupled standard maps, Eq. (2) with $\xi_{12} = 0$: (a) $K_1 = -2.25$ and $(p_2,q_2) = (0,0)$. The regular island (red and cyan) contains a 4 : 1 resonance (orange). Chaotic orbits (blue dots) appear outside of the regular island and inside a thin chaotic layer around the 4 : 1 resonance. (b) $K_2 = -3.0$ and $(p_1,q_1) = (0,0)$.

intersection), 1 (tangential intersection), 2 or more points. Periodic orbits, however, will typically not be in the slice.

As a concrete example we consider the prototypical system of two coupled standard maps [44],

$$\begin{aligned} p_1' &= p_1 + \frac{K_1}{2\pi}\sin(2\pi q_1') + \frac{\xi_{12}}{2\pi}\sin[2\pi(q_1' + q_2')] \\ p_2' &= p_2 + \frac{K_2}{2\pi}\sin(2\pi q_2') + \frac{\xi_{12}}{2\pi}\sin[2\pi(q_1' + q_2')] \\ q_1' &= q_1 + p_1 \\ q_2' &= q_2 + p_2, \end{aligned} \tag{2}$$

where $p_1,p_2,q_1,q_2 \in [-1/2,1/2)$ and periodic boundary conditions are imposed in each coordinate. The parameters K_1 and K_2 control the nonlinearity of the individual 2D standard maps in (p_1,q_1) and (p_2,q_2), respectively. The parameter ξ_{12} introduces a coupling between the two degrees of freedom. We choose as parameters of the uncoupled standard maps $K_1 = -2.25$ and $K_2 = -3.0$ such that at each of the origins $(p_1,q_1) = (0,0)$ and $(p_2,q_2) = (0,0)$ one has an elliptic fixed point; see Fig. 2. Note that for positive values of K_1 and K_2 the phase space would be shifted by $1/2$ in the q_1 and q_2 directions. In both cases, Figs. 2(a) and 2(b), one has a large regular region formed by invariant tori (red lines), which is surrounded by a region formed by chaotic orbits (blue dots). For $K_1 = -2.25$ the regular island contains a large 4 : 1 resonance. Note that the regular tori form absolute barriers to the motion, such that orbits starting in the chaotic region cannot enter the regular island and vice versa. For example, the blue chaotic orbit surrounding the 4 : 1 resonance in Fig. 2(a) is not dynamically connected to the large chaotic region also shown in blue.

We choose a strong coupling $\xi_{12} = 1.0$ to obtain a generic 4D phase space, which is far from being integrable. In this case the origin $\vec{u}_{\rm fp} = (p_1,p_2,q_1,q_2) = (0,0,0,0)$ remains an elliptic-elliptic fixed point, which follows from linearization [1,67–69].

We use the slice condition $p_2^* = 0$; see the Appendix for a variation of p_2^* and other choices. By numerically iterating several initial conditions until for each of them 8 000 points are contained in the 3D phase-space slice, we obtain Fig. 1. Chaotic trajectories lead to sequences of irregularly spread points; examples are shown as blue dots. Regular tori, which generically are 2D objects in the 4D phase space, appear as 1D lines in the 3D phase-space slice. They are shown in red, cyan, violet, pink, green, orange, and brown, depending on which structure in phase space they belong to. All these structures are given by families of 2D tori forming approximately 4D volumes with a 3D surface toward the chaotic domain if we neglect the Arnold web and the fractal structure of phase space. The initial conditions leading to the 1D lines shown in Fig. 1 are chosen such that they sample the surface of these structures in phase space evenly. This is accomplished by choosing the initial conditions manually based on FLI calculations [70]; see Sec. II B 3. By not starting orbits in the inside of the regular regions or too close to each other one ensures a clear representation of the underlying phase-space structures.

The regular tori in Fig. 1 appear to form a kind of *regular region* embedded in the large chaotic sea, similar to the case of a two-dimensional map. However, it is important to emphasize that this regular region is actually not a region but just a collection of regular tori with chaotic trajectories interspersed on arbitrarily fine scales. One such chaotic orbit is shown as a dense cloud of blue dots. The crucial difference between 2D and 4D maps is that this blue orbit in the chaotic layer will eventually spread into the main chaotic sea if iterated long enough. As regular tori are no longer absolute barriers in phase space [1], the thin chaotic zones and the main chaotic sea are connected with each other. Thus, all such chaotic trajectories close to the center will eventually enter the outer chaotic sea. Regular orbits of the central region are shown in red in Fig. 1. Other structures given by regular tori are indicated in different colors. Most of them appear twice (cyan) or four times (violet). This general feature of tori in 3D phase-space slices of a 4D phase space can be understood from an analogy in 3D space: Here, a 2D section of a 2D torus will typically give two 1D lines. Furthermore, there are two groups of tori (orange and brown), which are in the vicinity of two elliptic-elliptic period-7 orbits. [This is analogous to the case of a 2D map with a resonance chain; see Fig. 2(a).] Note that in each case only three points are close enough to the considered 3D phase-space slice such that their surrounding tori are visible in the slice. The other four points are further away; see Appendix 1. The orange structure will be investigated in detail in Appendix 3 b.

Figure 1 together with its rotated view [42] demonstrates that using a single 3D phase-space slice provides a lot of insight into the structures in phase space, in particular their relative locations are revealed and sizes can be inferred by varying the slice condition. This information is essential to predict the number of quantum eigenfunctions that localize in the different subregions of phase space; see Sec. III.

B. Comparison with other methods

We now compare the 3D phase-space slices with other common methods, namely 3D projections of orbits, the frequency analysis, and a chaos indicator. It turns out that they provide a complementary view of the classical phase-space structures. However, only the 3D phase-space slices allow for a visualization of quantum eigenstates in comparison with individual regular tori; see Sec. III.

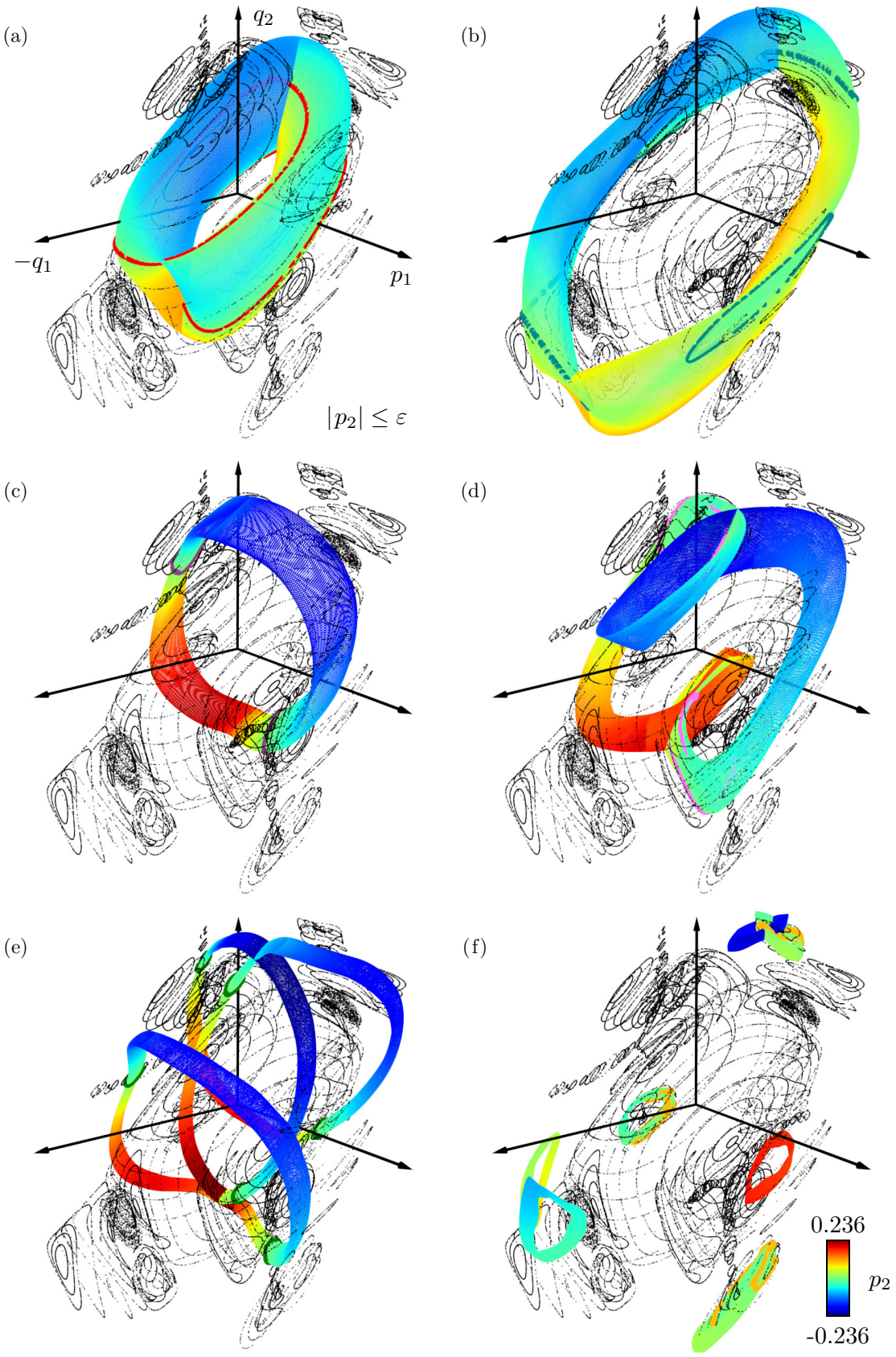

FIG. 3. (Color online) 3D phase-space slice for $|p_2| \leqslant \varepsilon$ of two coupled standard maps with 3D projections for different regular tori from Fig. 1: (a) red, (b) cyan, (c) violet, (d) pink, (e) green, and (f) orange. For the projection, the p_2 coordinate is encoded in color corresponding to the color bar. For a rotating view see the Supplemental Material [42].

1. 3D projections

Using 3D phase-space slices provides a global view of the geometry of the underlying 4D phase space by displaying several objects in the same plot. Alternatively, one can concentrate on one or few orbits and display all points by a 3D projection [43] and encode the value of the projected coordinate by a color scale; see Fig. 3. This approach has been called *method of color and rotation*; see Refs. [51,52,71]. The plots of the orbit projections reveal the underlying topology, i.e., which structures of the 3D phase-space slice Γ_ε (black) are connected. Figures 3(a)–3(c) show projected orbits belonging to the red, cyan, and violet region from Fig. 1. The projection shows that they indeed share the same topology. A closer investigation reveals that the torus (pink) shown in Fig. 3(d) is also of the same type and just bent in a more complicated way. The highlighted tori shown in Figs. 3(a)–3(d) have been called *rotational* [50,52].

Figure 3(e) shows the projection of an orbit from the green structure around the central regular region. Such tori have been called *tube tori* [50,52]. A frequency analysis, see Sec. II B 2, shows that the orbits of the green structure belong to the stable vicinity of the elliptic $-1:3:0$ rank-1 resonance [72]. Hence, we conclude that the tube tori result from coupled rank-1 resonances.

Finally, Fig. 3(f) shows the projection of an orange orbit from the elliptic-elliptic vicinity of the period-7 orbit of Fig. 1. Seven parts can be seen in the projection at the same time, while just three fulfill the slice condition of Fig. 1.

Only one or a few orbits can be displayed simultaneously using 3D projections, while many can be visualized in the 3D phase-space slice. Hence, using 3D phase-space slices and projections of orbits in combination is very instructive for the understanding of higher-dimensional maps.

2. Frequency analysis

We now compare the 3D phase-space slices with the frequency analysis [53–56]. This method associates each regular torus with its two fundamental frequencies $(\nu_1,\nu_2) \in [0,1[^2$, which are displayed in the 2D frequency plane; see Fig. 4. In the plot, the black points represent regular tori obtained by starting 10^8 initial conditions (with randomly chosen $p_1,p_2 \in [-0.2,0.2]$ and $q_1,q_2 \in [-0.2,0.2]$) in the 4D phase space. Note that for strongly coupled maps far from integrability a sampling on 2D planes is not sufficient as this will typically miss some regions with regular motion. Each frequency pair is calculated from $N = 4\,096$ iterations using a fast, analytical interpolation method (Sec. 4.2.4 in Ref. [73]). The error of this method scales with N^{-4} like the original method of Laskar [54]. To decide whether an orbit is regular we use the frequency criterion

$$\max(|\nu_1 - \tilde{\nu}_1|, |\nu_2 - \tilde{\nu}_2|) < 10^{-7}, \tag{3}$$

where the frequency pair $(\tilde{\nu}_1,\tilde{\nu}_2)$ is calculated from N further iterations. Note that the frequencies (ν_1,ν_2) are only defined up to a unimodular transformation (Sec. 15 in Ref. [74] and Refs. [75,76]). Using the 3D phase-space slices we can choose the frequencies consistently such that regular tori, which are close in phase space, are also close in the frequency plane. Explicitly, we make the following transformations: (i) if $\nu_i > 0.5$ then $\nu_i \mapsto 1 - \nu_i$, (ii) if $\nu_2 > \nu_1$ then $(\nu_1,\nu_2) \mapsto (\nu_2,\nu_1)$, (iii) for tori of the type shown in Fig. 3(d) with $\nu_2 > 0.25$ we use $(\nu_1,\nu_2) \mapsto (\nu_1,-4\nu_1 + \nu_2)$. The resulting frequency pairs reside in a small region of the frequency plane; see Fig. 4.

Additionally, the frequencies of the regular tori shown in Fig. 1 are displayed as squares with the corresponding color. This provides a connection between phase-space structures and areas in the frequency plane; e.g., the red points indicate that the area to the right corresponds to the central regular region. In fact, the linearization of the central elliptic-elliptic fixed point $\vec{u}_{\text{fp}}$ gives frequencies $(\nu_1,\nu_2) = (0.30632, 0.12173)$, which coincide with the rightmost tip in the frequency plane. The sharp edges emanating from the tip correspond to elliptic 1D tori, i.e., the limiting case of 2D tori for which one action becomes zero [77].

The frequency plane is organized by rank-1 resonance lines, on which the frequencies fulfill [54]

$$m_1\nu_1 + m_2\nu_2 = n \tag{4}$$

with m_1,m_2,n being integers. The most important ones are displayed in Fig. 4, abbreviating Eq. (4) by $m_1 : m_2 : n$. We stress that the resonance lines lead to gaps in the 4D phase space, clearly visible in the 3D phase-space slices; see Fig. 1. For example, the $-1:2:0$ resonance separates the red and the cyan region and the $3:1:1$ resonance separates the red and the pink region. The tori of the type shown in Fig. 3(d) (green in Fig. 1) demonstrate an advantage of the 3D phase-space slices: Performing a frequency analysis for these tori gives frequency pairs far away from the frequency region shown in Fig. 4. If one ignores a fundamental frequency with small amplitude and instead chooses two frequencies with large amplitude, the frequency pairs reside within the frequency region displayed in Fig. 4. However, they collapse on the resonance line $-1:3:0$.

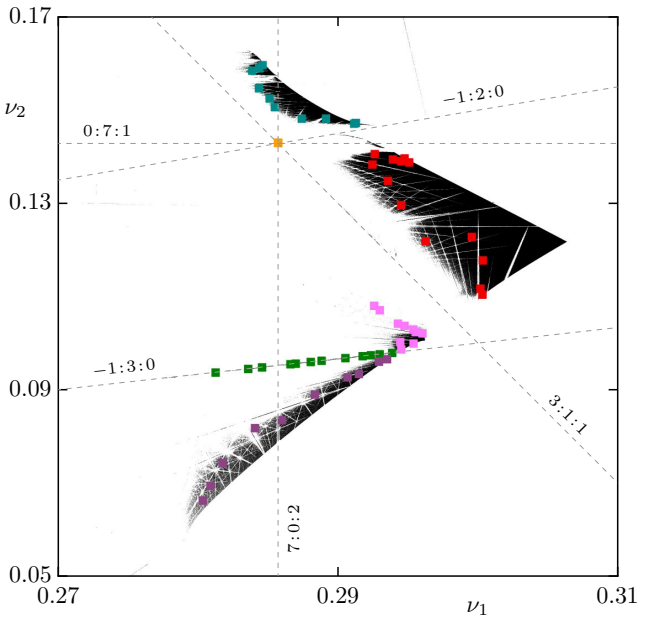

FIG. 4. (Color online) Frequency plane of two coupled standard maps at strong coupling $\xi_{12} = 1.0$. The colored squares correspond to the colored regular tori of Fig. 1. The black points correspond to additional regular tori.

In contrast, the representation of these tori in the 3D phase-space slice highlights both their relative location to other tori and that they are a two-parameter family of tori. The same is also true for the tori in the vicinity of the elliptic-elliptic period-7 orbits (orange, brown in Fig. 1). Choosing two frequencies with large amplitude in this case results in all frequency pairs collapsing to the point $(\nu_1,\nu_2) = (2/7,1/7)$.

These results demonstrate how the frequency plane with its resonance lines relates to the structures of the 4D phase space. The 3D phase-space slices reveal the topology and geometrical relevance of the resonance gaps. In particular, the 3D phase-space slices help to consistently assign frequencies to the regular tori in systems that are far away from integrability.

3. *Fast Lyapunov indicator*

We now compare the 3D phase-space slices with one example of a chaos indicator. Such chaos indicators associate with each initial condition a value describing the chaoticity of the corresponding trajectory [63–65]. We consider as an example the FLI [45,61,62]; see Fig. 5. To interpret the results of this indicator we calculate a histogram for a set of initial conditions in the 4D phase space. Small values correspond to regular motion and large values correspond to chaotic motion, which allows for adjusting the color scale; see Fig. 5. In this plot the FLI is displayed on three mutually perpendicular planes. These are placed such that most of the regular region is visible. The FLI is calculated using 4 096 iterations averaging over the last 50 values. The initial tangent vector is $[1, 1, 0.5\,(\sqrt{5}-1), 1]$ inspired by Ref. [70]. The color scale is chosen such that red regions coincide with regions of regular motion as can be seen from the orbits (black) in the 3D phase-space slice. Regions with intermediate FLI values are shown in green. Large FLI values correspond to strongly chaotic motion and are shown in blue.

Such a FLI representation is also useful for selecting regular orbits for the 3D phase-space slice. For Fig. 1, orbits from the border of the regular regions are used.

Another application of the FLI is the estimation of the size of the regular region. For this one starts trajectories on a grid in the 4D phase space and determines the fraction of orbits with a small FLI value, i.e., corresponding to the red regions of Fig. 5. Using 128^4 initial points and a maximum FLI value of 30 we find the approximate regular phase-space fraction to be 1.4×10^{-3}. Quantum mechanically this gives an estimate of the number of regular eigenstates; see Sec. III C.

Figure 5 shows that the plot for the regular tori in the 3D phase-space slices complements the plot of chaos indicators like the FLI. An advantage of 3D phase-space slices is that the geometry of individual tori is visible, which is particularly important when considering the quantized map, for which regular eigenstates concentrate on such tori.

III. STRUCTURE OF QUANTUM STATES

By means of the 3D phase-space slices, we are able to relate the quantum mechanical properties of higher-dimensional systems with the underlying classical structures. For this we first introduce the corresponding quantum map and the computation of eigenstates. Then the Husimi representation of eigenstates is visualized on the 3D phase-space slices to investigate the semiclassical eigenfunction hypothesis.

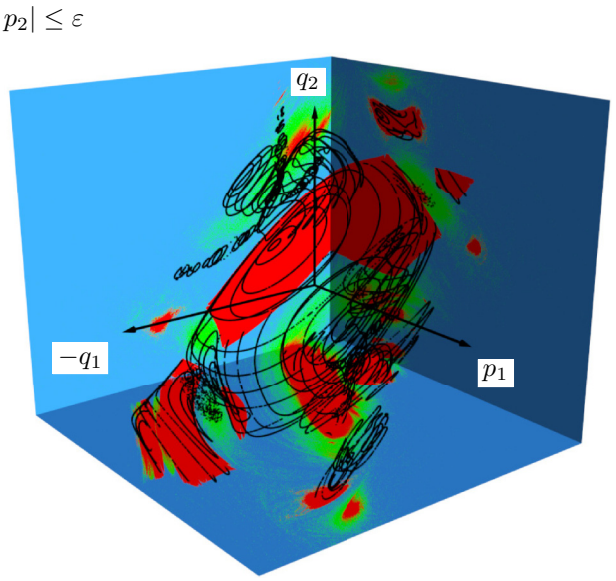

FIG. 5. (Color online) 3D phase-space slice for $|p_2| \leqslant \varepsilon$ of two coupled standard maps at strong coupling $\xi_{12} = 1.0$ with three 2D FLI planes. The color map is chosen such that points with FLI < 30 are shown in red, points with FLI > 150 are shown in blue, and intermediate values are marked green. The three planes are chosen away from the central elliptic-elliptic fixed point for better visibility. For a rotating view see the Supplemental Material [42].

A. Quantized map

The classical map Eq. (2) arises from the stroboscopic view of a kicked Hamiltonian of the form

$$H(\vec{p},\vec{q}\,) = T(\vec{p}\,) + V(\vec{q}\,)\sum_{n\in\mathbb{Z}}\delta(t-n), \tag{5}$$

where the period of the driving is 1. Quantum mechanically the time evolution

$$|\psi(t+1)\rangle = \hat{U}|\psi(t)\rangle, \tag{6}$$

of a state $|\psi(t)\rangle$ after one time period is fully determined by the unitary operator $\hat{U}$. The usual quantization for 2D maps, see, e.g., Refs. [78–81], straightforwardly carries over to the 4D case, see, e.g., Refs. [82,83]. Explicitly we have

$$\hat{U} = \exp\left[-\frac{\mathrm{i}}{\hbar_{\mathrm{eff}}}V(\hat{\vec{q}}\,)\right]\exp\left[-\frac{\mathrm{i}}{\hbar_{\mathrm{eff}}}T(\hat{\vec{p}}\,)\right], \tag{7}$$

where $V(\vec{q}\,) = \frac{K_1}{4\pi^2}\cos(2\pi q_1) + \frac{K_2}{4\pi^2}\cos(2\pi q_2) + \frac{\xi_{12}}{4\pi^2}\cos[2\pi(q_1+q_2)]$ and $T(\vec{p}\,) = \frac{1}{2}(p_1^2+p_2^2)$. Here, $h_{\mathrm{eff}} = 2\pi\hbar_{\mathrm{eff}}$ is the effective Planck's constant, which is Planck's constant h divided by the fth root of the size of one unit cell $V_{\mathrm{fD}}^{\mathrm{unit\,cell}}$ in phase space,

$$h_{\mathrm{eff}} = \frac{h}{\left(V_{\mathrm{fD}}^{\mathrm{unit\,cell}}\right)^{1/f}}, \tag{8}$$

where in our case we have the number of degrees of freedom $f = 2$.

Of particular interest are the stationary states, i.e., the eigenstates $|\psi_j\rangle$ of $\hat{U}$, defined by

$$\hat{U}|\psi_j\rangle = \mathrm{e}^{\mathrm{i}\varphi_j}|\psi_j\rangle, \tag{9}$$

with the eigenphases φ_j. Due to the periodicity of the classical phase space in the p_i directions, one can express the time evolution operator $\hat{U}$ in a discrete position basis $|\vec{q}_{\vec{n}}\rangle \equiv |\vec{q}_{n_1,n_2}\rangle$ with $0 \leqslant n_i \leqslant N-1$, where N is the number of grid points in each direction. This gives rise to a N^2-dimensional Hilbert space and the quantization condition

$$h_{\mathrm{eff}} = \frac{1}{N}. \tag{10}$$

With this, the grid in position space reads

$$\vec{q}_{\vec{n}} = \vec{q}_0 + \frac{1}{N}\vec{n}, \tag{11}$$

with $\vec{q}_0 = (-1/2, -1/2)$.

Now we can express the propagator $\hat{U}$ by a finite $N^2 \times N^2$ unitary matrix (for even N),

$$\begin{aligned} U_{\vec{n}\vec{k}} &\equiv \langle \vec{q}_{\vec{n}}|\hat{U}|\vec{q}_{\vec{k}}\rangle \\ &= h_{\mathrm{eff}}^2\, \mathrm{e}^{-\frac{\mathrm{i}}{\hbar_{\mathrm{eff}}}V(\vec{q}_{\vec{n}})} \sum_{j_1=0}^{N-1}\sum_{j_2=0}^{N-1} \mathrm{e}^{-\frac{\mathrm{i}}{\hbar_{\mathrm{eff}}}[T(\vec{p}_{\vec{j}})+\vec{p}_{\vec{j}}(\vec{q}_{\vec{n}}-\vec{q}_{\vec{k}})]}, \end{aligned} \tag{12}$$

where $\vec{p}_{\vec{j}} = \vec{p}_0 + \frac{1}{N}\vec{j}$. Finding the solution of Eq. (9), i.e., the eigenphases and eigenstates of the system, therefore reduces to the numerical diagonalization of the unitary matrix Eq. (12). The matrix size scales like h_{eff}^{-2}, in contrast to 2D maps, where it scales like h_{eff}^{-1}. This shows that numerical studies of higher-dimensional systems in the semiclassical limit of small h_{eff} require much more computational effort.

B. Lanczos algorithm

For the semiclassical behavior of eigenstates, i.e., in the limit of small h_{eff}, we have to consider large matrices. This makes it necessary to use appropriate diagonalization schemes, which allow for computing a few rather than all eigenstates. One possibility is the Lanczos algorithm [84], which transforms U into tridiagonal form. The method is particularly efficient if the application of the unitary operator to a vector can be performed fast, in our case by a fast Fourier-transform as in Ref. [85]. This leads to a computational effort of $N^4 \ln N$ instead of N^6 for the direct diagonalization.

In order to use this approach for the computation of eigenstates concentrated on a specific region in the classical phase space, the initial vector of the Lanczos algorithm has to be chosen appropriately. Usually a random vector is used as the initial state $|\chi\rangle$. Instead we choose a coherent state $|\chi\rangle = |\mathrm{coh}(\vec{p}_0,\vec{q}_0)\rangle$,

$$\langle \vec{q}|\mathrm{coh}(\vec{p}_0,\vec{q}_0)\rangle = \frac{1}{\sqrt{\pi\hbar_{\mathrm{eff}}}} \exp\left(-\frac{(\vec{q}-\vec{q}_0)^2}{2\hbar_{\mathrm{eff}}} + \mathrm{i}\frac{\vec{p}_0\vec{q}}{\hbar_{\mathrm{eff}}}\right), \tag{13}$$

concentrated at a point $(\vec{p}_0,\vec{q}_0)$. By this it is possible to selectively calculate those eigenstates, which have a large overlap with $|\chi\rangle$: After the transformation to tridiagonal form we sequentially [86] calculate all eigenvectors $|\psi_j\rangle$. By construction of the Lanczos algorithm, the first component of each eigenvector gives the overlap with the initial coherent state $\langle\psi_j|\chi\rangle$. We select the states with largest overlap and transform them back to position space representation. Finally, one has to verify whether the resulting state really is an eigenstate as the Lanczos algorithm introduces spurious solutions due to round-off errors. As a criterion, the residuum

$$\|(\hat{U} - \mathrm{e}^{\mathrm{i}\varphi_j})|\psi_j\rangle\|^2 \tag{14}$$

is computed and we only consider states having a value smaller than 10^{-10}. Note that for weakly coupled systems the initial state for the Lanczos algorithm could, instead of a coherent state, also be a direct product of eigenstates of the uncoupled 2D systems.

C. Husimi representation of eigenstates

While the eigenstates of a 4D map can still be visualized in position representation, this does not allow for understanding where the eigenstates concentrate in phase space. One possible phase-space representation of a state is the Husimi representation (see Refs. [38,87,88] and references therein),

$$\mathsf{H}_\psi(\vec{p},\vec{q}\,) = \frac{1}{h_{\mathrm{eff}}^2}|\langle \mathrm{coh}(\vec{p},\vec{q}\,)|\psi\rangle|^2, \tag{15}$$

which is the projection of the state $|\psi\rangle$ onto coherent states $\mathrm{coh}(\vec{p}_0,\vec{q}_0)$, where also the periodicity of the phase space has to be taken into account by periodizing the coherent states.

To visualize the Husimi function on the 3D phase-space slice, i.e., $\mathsf{H}_\psi(p_1,p_2=0,q_1,q_2)$, semitransparent isosurfaces are used with a color association such that red corresponds to high intensity; see Fig. 6. While classical orbits are displayed in a 3D phase-space slice Γ_ε, the Husimi function is computed on the hyperplane Γ. As the fraction of the volume of the regular phase-space region can be estimated to be 1.4×10^{-3}, we expect for $h_{\mathrm{eff}} = \frac{1}{500}$ approximately 350 regular and 249 650 chaotic eigenstates.

Figure 6(a) shows the "ground state" of the central regular region (red in Fig. 1), which concentrates around the elliptic-elliptic fixed point. It is approximately given by a Gaussian shape in the Husimi function H_ψ. In the position-space probability-density $|\psi(\vec{q}\,)|^2$, it is also approximately given by a Gaussian distribution. Figure 6(b) shows an excited state of the central region. Its Husimi function nicely shows that this state predominantly lives on the classical torus, which corresponds to two 1D lines in the 3D phase-space slice. The quantum numbers (4,6) of this state can be read off from the nodal lines in the position-space probability density.

Figures 6(c)–6(e) show eigenstates concentrating on more complicated phase-space structures, corresponding to the regular tori shown in Fig. 1 (pink, green, and orange). Note that the eigenstate concentrating on the period-7 orbit extends over both chains (orange and brown in Fig. 1). This is also the reason why the position-space probability-density plot shows eight maxima: These are given by two period-7 orbits, each of which shows four distinct points in the projection onto the (q_1,q_2) plane. Finally, Fig. 6(f) shows a chaotic state, which is concentrated on the chaotic sea and decays rapidly into the regular region. Looking at the eigenstates on a logarithmic

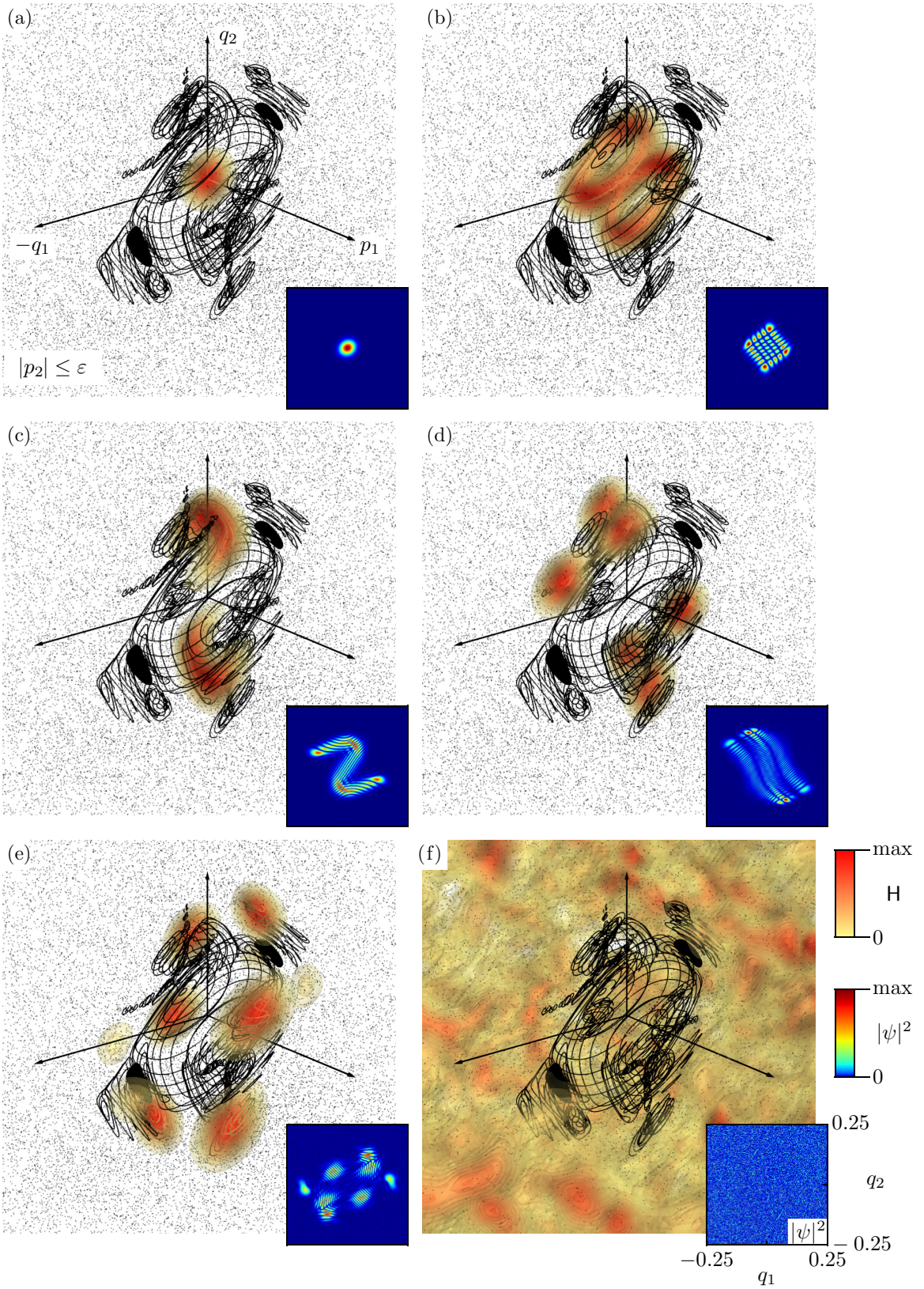

FIG. 6. (Color online) Husimi representation H of eigenstates of the time-evolution operator $\hat{U}$ for $h_{\text{eff}} = \frac{1}{500}$ in the 3D phase-space slice and position-space probability-density $|\psi|^2$ (insets). (a) Ground state $|\psi_{0,0}\rangle$ of the central regular region. (b) Excited state $|\psi_{4,6}\rangle$. (c) State concentrated on pink structure shown in Fig. 1. (d) State concentrated on green structure shown in Fig. 1. (e) State concentrated on vicinity of period-7 orbit (orange and brown structure in Fig. 1). (f) Chaotic eigenstate where the octant in the front has been removed for better visibility. For a rotating view see the Supplemental Material [42].

representation reveals tunneling tails of chaotic states into the regular region and of regular states into the chaotic sea (not shown).

Figure 6 clearly shows that the eigenstates either concentrate on regular tori or within the chaotic sea providing visual confirmation of the semiclassical eigenfunction hypothesis for 4D maps. This is made possible by the use of 3D phase-space slices.

IV. SUMMARY AND OUTLOOK

To understand the dynamics of 4D symplectic maps, we use 3D phase-space slices. They provide the basis for a similar level of understanding as for 2D maps. Such a visualization is of particular importance for generic systems being far away from integrability. Classically, the 3D phase-space slices reveal a regular region embedded in a large chaotic sea for the prototypical example of two coupled standard maps; see Fig. 1. The regular region consists of several substructures of different topology, which are separated by gaps. The geometrical relation of these substructures in phase space enables us to consistently assign frequencies to the regular tori and allows for interpreting the results of the frequency analysis. We identify resonance gaps by a combination of 3D phase-space slices and frequency analysis. Moreover, we conclude that the so-called tube tori result from coupled rank-1 resonances.

A comparison of the 3D phase-space slices with orbit projections and a chaos indicator shows that they nicely complement each other. However, an important motivation for the use of 3D phase-space slices is the investigation of quantum mechanical properties in higher-dimensional systems. To relate the structure of eigenstates with corresponding classical structures, the comparison has to be done in phase space. The 3D phase-space slices are best suited for this purpose, since they visualize both several individual orbits at the same time and the global geometry in phase space. We display several eigenstates of the time-evolution operator in the Husimi representation on the 3D phase-space slice together with classical orbits. By this we can confirm the semiclassical eigenfunction hypothesis, namely that eigenstates either concentrate on regular tori or in the chaotic region. Based on this, an investigation of dynamical tunneling between a regular and the chaotic region is possible.

The 3D phase-space slices also allow for displaying families of elliptic 1D tori that provide the skeleton around which the 2D tori are organized [21,77]. In the future, the 3D phase-space slices may be used to display invariant phase-space structures, such as 1D tori or stable and unstable manifolds of fixed points and periodic orbits. Another important application of 3D phase-space slices is the determination of those phase-space structures at which trapping of chaotic orbits occurs in systems far away from integrability [21]. These long-trapped orbits are the key to the understanding of power-law recurrence-time statistics.

We hope that the method of 3D phase-space slices will be useful for the understanding of the phase-space structure and the dynamics of 4D maps and possibly higher-dimensional systems.

ACKNOWLEDGMENTS

We thank Srihari Keshavamurthy and Peter Schlagheck for stimulating discussions. We further acknowledge discussions with Jacques Laskar, Haris Skokos, and Matthaios Katsanikas. We thank the Center for Information Services and High Performance Computing (ZIH Dresden) for access to the computing facilities. Furthermore, we acknowledge support by the Deutsche Forschungsgemeinschaft within the Forschergruppe 760 "Scattering Systems with Complex Dynamics." All 3D visualizations were created using MAYAVI [66].

APPENDIX: GENERAL 3D PHASE-SPACE SLICES

As only a part of phase space is visible in a 3D phase-space slice it is instructive to consider other 3D phase-space slices, e.g., by shifting the slice condition, choosing other coordinates for the slice, or by using adapted nonorthogonal coordinates. This is illustrated in the following sections.

1. Shifting the slice condition

A global view of the dynamics in the full phase space is obtained by varying the value of p_2^* of the slice condition Eq. (1). This is illustrated in the sequence of plots in Fig. 7, where $p_2^* = 0.0, -0.0875, -0.14, -0.1925$ is chosen and only regular tori are shown. Thereby, the slice condition p_2^* is shifted away from the fixed point ($p_2 = 0$) and we observe that the visible regular region shrinks and finally vanishes (not shown). The outermost tori at $p_2^* = 0$ (violet and cyan) persist the longest. Both features can be understood from a 2D analogy where a 1D slice of a regular island is shifted away from the fixed point. Furthermore, we observe the appearance of two other members of the period-7 subregion (orange and brown) in Figs. 7(b) and 7(d). Varying p_2^* to positive values yields qualitatively the same sequence of pictures.

While typically tori appear twice in the 3D phase-space slice, under variation of p_2^* every pair of 1D lines finally coalesces into a single 1D line before it disappears; see, e.g., central violet tori in Fig. 7(d). This can again be understood from an analogy in 3D space when a 2D section is shifted out of a 2D torus.

2. Slice condition with different coordinates

Instead of choosing p_2 as the coordinate for the slice condition Eq. (1), one can choose any of the other coordinates to obtain a complementary view of the underlying phase space. If, however, the system under consideration is strongly coupled, then the single degrees of freedom (p_i, q_i) are heavily intertwined. Therefore, usually none of the slices along any of the q_i or p_i has an advantage over any other possible choice.

Note that more generally one can define a rotated 3D phase-space slice by the slice condition

$$|\vec{u} \cdot \vec{n} - D| \leqslant \varepsilon, \tag{A1}$$

for points $\vec{u}$ in phase space, where $\vec{n}$ is the normal vector to the chosen slice and D is the distance of the slice to the origin.

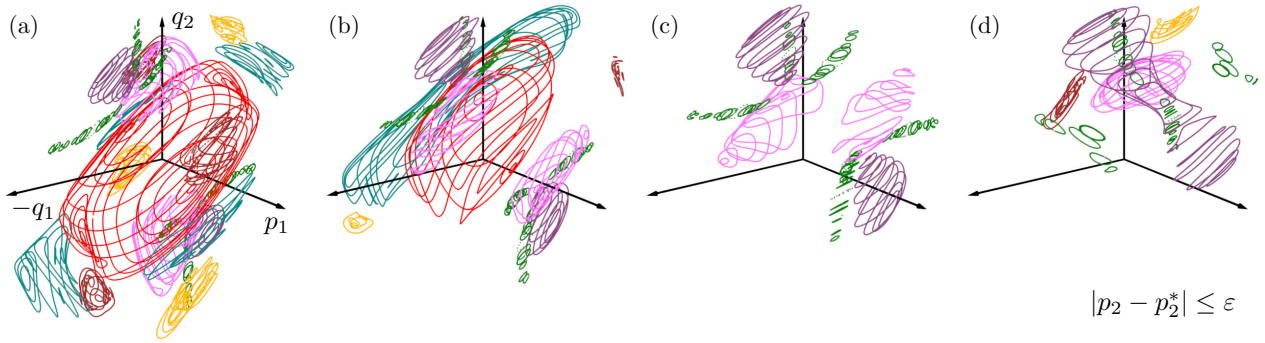

FIG. 7. (Color online) 3D phase-space slices for $|p_2 - p_2^*| \leqslant \varepsilon$ of two coupled standard maps at strong coupling $\xi_{12} = 1.0$ for varying $p_2^* = 0.0, -0.0875, -0.14$, and -0.1925, (a)–(d), respectively. The color of the orbits is the same as in Fig. 1. For a rotating view of each picture and a video showing the variation of p_2^* see the Supplemental Material [42].

3. Adapted 3D phase-space slices

When focusing on the vicinity of fixed points $\vec{u}_{\mathrm{fp}}$ or periodic orbits $\vec{u}_{\mathrm{p}}$, one can choose a more appropriate slice than the one given by Eq. (1). For this we use the properties of the linearized system at $\vec{u}_{\mathrm{fp}}$ or $\vec{u}_{\mathrm{p}}$ to define the phase-space slice. For simplicity we will describe this approach for fixed points as it trivially extends to periodic orbits.

For an elliptic-elliptic fixed point $\vec{u}_{\mathrm{fp}}$, the four eigenvectors appear in pairs $(\vec{\chi}_1, \vec{\chi}_1^*)$ and $(\vec{\chi}_2, \vec{\chi}_2^*)$ corresponding to the eigenvalue pairs (λ_1, λ_1^*) and (λ_2, λ_2^*) [1]. The spaces spanned by the pairs

$$\begin{array}{ll} \vec{e}_\alpha \propto \mathrm{Re}\ \vec{\chi}_1 & \vec{e}_\gamma \propto \mathrm{Re}\ \vec{\chi}_2 \\ \vec{e}_\beta \propto \mathrm{Im}\ \vec{\chi}_1 & \vec{e}_\delta \propto \mathrm{Im}\ \vec{\chi}_2 \end{array} \quad \text{and} \tag{A2}$$

are invariant under the linearized dynamics. In order to introduce a more appropriate slice for $\vec{u}_{\mathrm{fp}}$, we first note that every point $\vec{u}$ in phase space can be uniquely decomposed into

$$\vec{u} = \alpha\vec{e}_\alpha + \beta\vec{e}_\beta + \gamma\vec{e}_\gamma + \delta\vec{e}_\delta, \tag{A3}$$

using the dual basis to the vectors from Eq. (A2): Given the matrix built columnwise from the vectors $\vec{e}_\alpha, \vec{e}_\beta, \vec{e}_\gamma, \vec{e}_\delta$ the dual basis vectors $\vec{\tilde{e}}_\alpha, \vec{\tilde{e}}_\beta, \vec{\tilde{e}}_\gamma, \vec{\tilde{e}}_\delta$ can be obtained numerically via

$$\left(\vec{\tilde{e}}_\alpha | \vec{\tilde{e}}_\beta | \vec{\tilde{e}}_\gamma | \vec{\tilde{e}}_\delta\right) = \left(\vec{e}_\alpha | \vec{e}_\beta | \vec{e}_\gamma | \vec{e}_\delta\right)^{-1^T}. \tag{A4}$$

This provides the components $\alpha = \vec{\tilde{e}}_\alpha \cdot \vec{u}, \beta = \vec{\tilde{e}}_\beta \cdot \vec{u}, \gamma = \vec{\tilde{e}}_\gamma \cdot \vec{u}, \delta = \vec{\tilde{e}}_\delta \cdot \vec{u}$. Although the vectors $\vec{e}_\alpha, \vec{e}_\beta, \vec{e}_\gamma, \vec{e}_\delta$ are nonorthogonal, we can use any subset of them to define an adapted 3D phase-space slice: For example, using the slice condition

$$|\delta - D| \leqslant \varepsilon, \tag{A5}$$

the coordinates α, β, and γ can be plotted into an orthogonal 3D coordinate system. This slice is orthogonal to the dual vector $\vec{\tilde{e}}_\delta$. Although this 3D plot is not angle-preserving, it displays the features of the phase space in the vicinity of the elliptic-elliptic fixed point $\vec{u}_{\mathrm{fp}}$ very clearly.

Moreover, these adapted 3D phase-space slices could also be used to examine the vicinities of elliptic-hyperbolic and

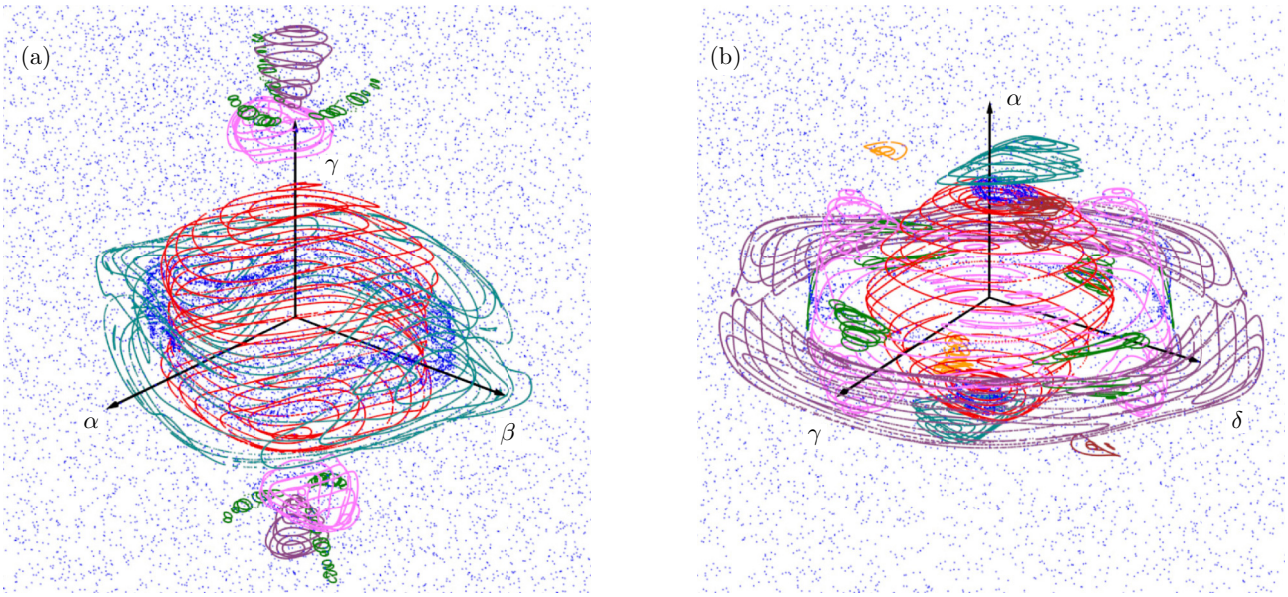

FIG. 8. (Color online) Adapted 3D phase-space slices of two coupled standard maps for the vicinity of the central fixed point $\vec{u}_{\mathrm{fp}}$, for (a) coordinates α, β, γ and slice condition $|\delta| \leqslant \varepsilon$ and (b) coordinates α, γ, δ and slice condition $|\beta| \leqslant \varepsilon$. Shown are the orbits from Figs. 1 and 7 using the same color code. For a rotating view see the Supplemental Material [42].

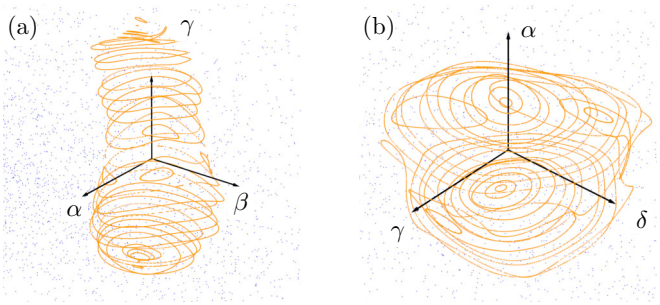

FIG. 9. (Color online) Adapted 3D phase-space slices of two coupled standard maps for the vicinity of an elliptic-elliptic period-7 orbit, with slice conditions (a) $|\delta| \leqslant \varepsilon$ and (b) $|\beta| \leqslant \varepsilon$. For a rotating view see the Supplemental Material [42].

hyperbolic-hyperbolic points. Note that adapted 3D phase-space slices are equivalent to slices through the phase space of a system after a normal form transformation. We now briefly discuss two situations for using adapted 3D phase-space slices:

a. Elliptic-elliptic fixed points. First, we consider the central elliptic-elliptic fixed point $\vec{u}_{\mathrm{fp}}$. Figures 8(a) and 8(b) show the results for the slice conditions $|\delta| \leqslant \varepsilon$ and $|\beta| \leqslant \varepsilon$. In Fig. 8(a) the degree of freedom spanned by $(\vec{e}_\alpha, \vec{e}_\beta)$ is completely visible, and in Fig. 8(b) the one spanned by $(\vec{e}_\gamma, \vec{e}_\delta)$ is completely visible. Note that the slice conditions $|\gamma| \leqslant \varepsilon$ or $|\alpha| \leqslant \varepsilon$ lead to qualitatively similar pictures, respectively.

Both Figs. 8(a) and 8(b) give a very clear representation of the regular phase-space region where the central part (red) shows 2D tori as two separate 1D lines each. They are nicely stacked vertically on top of each other as would be the case for an uncoupled, purely integrable system. Figures 8(a) and 8(b) together provide a complementary visualization of the 4D phase space: Structures which are concentrated on the α-β plane in Fig. 8(a) are localized along the α axis in the other slice in Fig 8(b) and analogously objects on the γ-δ plane lie on the γ axis in Fig. 8(a). For example, the cyan part of the regular region (and also the blue chaotic orbit) in Fig. 8(a) is above and below in α direction in Fig. 8(b). This is true the other way around for the violet and pink continuation of the central regular region and the green structure.

The adapted 3D phase-space slices yield very organized phase-space pictures, even though their advantage is present mainly locally, close to the fixed point used for defining the slice. Figure 8 shows that away from the central elliptic-elliptic fixed point $\vec{u}_{\mathrm{fp}}$, the phase-space structures become more involved, which is similar to 2D maps if one moves outside of the center of the main island (compare with Fig. 2). Also, not all phase-space structures have to be present; e.g., the stable vicinity of the period-7 orbit is shown in orange in Fig. 8(b) but is not visible in Fig. 8(a).

b. Elliptic-elliptic periodic orbits. Suitably adapted phase-space slices can also be used to study periodic orbits of higher period, in order to see the self-similar structure of the phase space. In Fig. 1 the vicinity of an elliptic-elliptic periodic orbit of period 7 is shown in orange. One of its points is located at $\vec{u}_{\mathrm{p}} = (0.0, 0.0, 0.083438087, 0.118666288)$ and is therefore already visible in Fig. 1. For this point the adapted 3D phase-space slice is shown in Figs. 9(a) and 9(b): The stable vicinity now looks very similar to the central regular region in Fig. 8 as it is again given by 1D lines inside the 3D phase-space slice vertically stacked on top of each other. This is not obvious from the nonadapted 3D phase-space slices shown in Fig. 1. One could proceed from this sevenfold map further down in the hierarchy of periodic orbits.

Note that the fundamental frequencies of the tori shown in Fig. 9 lie far away from the frequency region shown in Fig. 4. Taking the frequencies with the largest amplitude leads to $(\nu_1, \nu_2) = (2/7, 1/7)$ in Fig. 4.

[1] A. J. Lichtenberg and M. A. Liebermann, *Regular and Chaotic Dynamics*, 2nd ed. (Springer-Verlag, New York, 1992).
[2] S. Udry and D. Pfenniger, Astron. Astrophys. **198**, 135 (1988).
[3] J. Laskar, Icarus **88**, 266 (1990).
[4] P. M. Cincotta, New Astron. Rev. **46**, 13 (2002).
[5] H. S. Dumas and J. Laskar, Phys. Rev. Lett. **70**, 2975 (1993).
[6] K. Richter and D. Wintgen, Phys. Rev. Lett. **65**, 1965 (1990).
[7] P. Schlagheck and A. Buchleitner, Physica D **131**, 110 (1999).
[8] S. Keshavamurthy, Int. Rev. Phys. Chem. **26**, 521 (2007).
[9] H. Waalkens, R. Schubert, and S. Wiggins, Nonlinearity **21**, R1 (2008).
[10] É. V. Shuryak, Zh. Eksp. Teor. Fiz **71**, 2039 (1976) [Sov. Phys. JETP **44**, 1070 (1976)].
[11] V. Y. Demikhovskii, F. M. Izrailev, and A. I. Malyshev, Phys. Rev. Lett. **88**, 154101 (2002).
[12] A. Malyshev and L. Chizhova, J. Exp. Theor. Phys. **110**, 837 (2010).
[13] S. Adachi, M. Toda, and K. Ikeda, Phys. Rev. Lett. **61**, 659 (1988).
[14] B. Gadway, J. Reeves, L. Krinner, and D. Schneble, Phys. Rev. Lett. **110**, 190401 (2013).
[15] V. I. Arnold, Dokl. Akad. Nauk SSSR **156**, 9 (1964) [Sov. Math. Dokl. **5**, 581 (1964)].
[16] B. V. Chirikov, Phys. Rep. **52**, 263 (1979).
[17] K. Kaneko and R. J. Bagley, Phys. Lett. A **110**, 435 (1985).
[18] M. Ding, T. Bountis, and E. Ott, Phys. Lett. A **151**, 395 (1990).
[19] E. G. Altmann and H. Kantz, Europhys. Lett. **78**, 10008 (2007).
[20] D. L. Shepelyansky, Phys. Rev. E **82**, 055202 (2010).
[21] S. Lange, Diploma thesis, Technische Universität Dresden, Fachrichtung Physik (2012).
[22] S. Gekle, J. Main, T. Bartsch, and T. Uzer, Phys. Rev. Lett. **97**, 104101 (2006).
[23] R. Paškauskas, C. Chandre, and T. Uzer, Phys. Rev. Lett. **100**, 083001 (2008).
[24] A. Luque and J. Villanueva, Nonlinearity **24**, 1033 (2011).
[25] I. C. Percival, J. Phys. B **6**, L229 (1973).
[26] M. V. Berry, J. Phys. A **10**, 2083 (1977).
[27] A. Voros, in *Stochastic Behavior in Classical and Quantum Hamiltonian Systems*, Vol. 93 of Lecture Notes in Physics, edited by G. Casati and J. Ford (Springer-Verlag, Berlin, 1979), pp. 326–333.
[28] A. I. Shnirelman, Usp. Math. Nauk **29**, 181 (1974).

[29] S. Zelditch, Duke. Math. J. **55**, 919 (1987).
[30] Y. Colin de Verdière, Commun. Math. Phys. **102**, 497 (1985).
[31] L. Hufnagel, R. Ketzmerick, M.-F. Otto, and H. Schanz, Phys. Rev. Lett. **89**, 154101 (2002).
[32] A. Bäcker, R. Ketzmerick, and A. G. Monastra, Phys. Rev. Lett. **94**, 054102 (2005).
[33] A. Bäcker, R. Ketzmerick, and A. G. Monastra, Phys. Rev. E **75**, 066204 (2007).
[34] A. Ishikawa, A. Tanaka, and A. Shudo, Phys. Rev. Lett. **104**, 224102 (2010).
[35] M. Michler, A. Bäcker, R. Ketzmerick, H.-J. Stöckmann, and S. Tomsovic, Phys. Rev. Lett. **109**, 234101 (2012).
[36] S. D. Frischat and E. Doron, J. Phys. A **30**, 3613 (1997).
[37] G. Veble, M. Robnik, and J. Liu, J. Phys. A **32**, 6423 (1999).
[38] A. Bäcker, in Ref. [41], pp. 91–144.
[39] A. Bäcker, S. Fürstberger, and R. Schubert, Phys. Rev. E **70**, 036204 (2004).
[40] J. Marklof, S. O'Keefe, and S. Zelditch, Nonlinearity **18**, 277 (2005).
[41] M. Degli Esposti and S. Graffi, eds., *The Mathematical Aspects of Quantum Maps*, Vol. 618 of Lecture Notes in Physics (Springer-Verlag, Berlin, 2003).
[42] See Supplemental Material at http://link.aps.org/supplemental/10.1103/PhysRevE.89.022902 for videos with rotating camera position.
[43] C. Froeschlé, Astron. Astrophys. **4**, 115 (1970).
[44] C. Froeschlé, Astron. Astrophys. **16**, 172 (1972).
[45] C. Froeschlé and E. Lega, Celest. Mech. Dynam. Astronomy **78**, 167 (2000).
[46] D. Pfenniger, Astron. Astrophys. **150**, 97 (1985).
[47] Ch. Skokos, G. Contopoulos, and C. Polymilis, Celest. Mech. Dynam. Astronomy **65**, 223 (1997).
[48] L. Martinet and P. Magnenat, Astron. Astrophys. **96**, 68 (1981).
[49] P. Magnenat, Celestial Mech. **28**, 319 (1982).
[50] M. N. Vrahatis, T. C. Bountis, and M. Kollmann, Int. J. Bifurcation Chaos **6**, 1425 (1996).
[51] P. A. Patsis and L. Zachilas, Int. J. Bifurcation Chaos **4**, 1399 (1994).
[52] M. Katsanikas and P. A. Patsis, Int. J. Bifurcation Chaos **21**, 467 (2011).
[53] C. Martens, M. Davis, and G. Ezra, Chem. Phys. Lett. **142**, 519 (1987).
[54] J. Laskar, Physica D **67**, 257 (1993).
[55] C. Chandre, S. Wiggins, and T. Uzer, Physica D **181**, 171 (2003).
[56] A. Sethi and S. Keshavamurthy, Mol. Phys. **110**, 717 (2012).
[57] A. Bazzani, L. Bongini, and G. Turchetti, Phys. Rev. E **57**, 1178 (1998).
[58] G. Benettin, L. Galgani, A. Giorgilli, and J.-M. Strelcyn, Meccanica **15**, 9 (1980).
[59] Ch. Skokos, Lect. Notes Phys. **790**, 63 (2010).
[60] C. Manchein, M. W. Beims, and J. M. Rost, Chaos **22**, 033137 (2012).
[61] C. Froeschlé, E. Lega, and R. Gonczi, Celest. Mech. Dynam. Astronomy **67**, 41 (1997).
[62] C. Froeschlé, M. Guzzo, and E. Lega, Science **289**, 2108 (2000).
[63] Ch. Skokos, J. Phys. A **34**, 10029 (2001).
[64] N. P. Maffione, L. A. Darriba, P. M. Cincotta, and C. M. Giordano, Celest. Mech. Dynam. Astronomy **111**, 285 (2011).
[65] E. E. Zotos, Nonlinear Dynamics **70**, 951 (2012).
[66] P. Ramachandran and G. Varoquaux, Comput. Sci. Eng. **13**, 40 (2011).
[67] J. E. Howard and R. S. MacKay, J. Math. Phys. **28**, 1036 (1987).
[68] J. E. Howard and H. R. Dullin, Phys. Lett. A **246**, 273 (1998).
[69] Ch. Skokos, Physica D **159**, 155 (2001).
[70] E. Lega, M. Guzzo, and C. Froeschlé, Physica D **182**, 179 (2003).
[71] C. Efthymiopoulos and M. Harsoula, Physica D **251**, 19 (2013).
[72] E. Todesco, Phys. Rev. E **50**, R4298 (1994).
[73] R. Bartolini, A. Bazzani, M. Giovannozzi, W. Scandale, and E. Todesco, Part. Accel. **52**, 147 (1996).
[74] M. Born, *The Mechanics of the Atom* (G. Bell and Sons, LTD, London, 1927).
[75] H. R. Dullin and J. D. Meiss, Chaos **13**, 1 (2003).
[76] S. Gekle, J. Main, T. Bartsch, and T. Uzer, Phys. Rev. A **75**, 023406 (2007).
[77] S. Lange, M. Richter, F. Onken, A. Bäcker, and R. Ketzmerick, arXiv:1311.7632.
[78] M. V. Berry, N. L. Balazs, M. Tabor, and A. Voros, Ann. Phys. **122**, 26 (1979).
[79] S.-J. Chang and K.-J. Shi, Phys. Rev. A **34**, 7 (1986).
[80] J. P. Keating, F. Mezzadri, and J. M. Robbins, Nonlinearity **12**, 579 (1999).
[81] M. Degli Esposti and S. Graffi, in Ref. [41], pp. 49–90.
[82] A. Rivas, M. Saraceno, and A. Ozorio de Almeida, Nonlinearity **13**, 341 (2000).
[83] A. Lakshminarayan, Phys. Rev. E **64**, 036207 (2001).
[84] J. K. Cullum and R. A. Willoughby, *Lanczos Algorithms for Large Symmetric Eigenvalue Computations* (Birkhäuser, Boston, 1985).
[85] R. Ketzmerick, K. Kruse, and T. Geisel, Physica D **131**, 247 (1999).
[86] This sequential computation relies on routines that calculate part of the spectrum and the corresponding eigenvectors $|\psi_j\rangle$. Here we used dstevr of a recent ATLAS implementation.
[87] K. Husimi, Proc. Phys. Math. Soc. Jpn. **22**, 264 (1940).
[88] S. Nonnenmacher and A. Voros, J. Stat. Phys. **92**, 431 (1998).